1. Characterization methods

Each of the synthesized materials were analyzed by X-ray diffraction pattern (XRD) in order to assess the crystalline phases. This was performed using the PANalytical X'Pert PROh-2h (PANalytical) scan system equipped with copper anode and an X'Celerator linear detector. The diffraction peaks were analyzed with High Score Plus software. For high resolution XRD, sample was placed in capillary and measured under transmission mode.

Study of the morphology of the obtained materials as well as EDS analysis was executed by scanning electron microscope Tescan SEM Vega3 fitted with Bruker XFlash 6-10 detector, with an accelerating voltage equal 20kV. High resolution image was obtained on Zeiss Gemini 460 with an accelerating voltage of 1.0kV

To evaluate the oxidation states and to probe the local geometries, ex-situ X-ray absorption (XAS) was performed at the Cr, Fe, Co, Ni, Cu, and Zn k-edge at the SuperXAS beamline at the Swiss Light Source (SLS) under transmission configuration.(1) The beam was collimated using a Si coated mirror at 2.9 mrad and subsequently monochromatised using channel cut Si 111 monochromator continuously oscillating with a 1 Hz frequency. Focussing of the monochromatic beam was performed using a Rh coated double focusing mirror with a beam spot size on the sample of 1 mm x 0.200 mm (HxV). The incident and transmitted flux was measured using 1 bar N_2 filled ion chamber for the Cr, Fe and Co edges and 2 bar N_2 for the Ni, Cu and Zn K-edges. Energy calibration was achieved using the associated reference foil measured simultaneously after the sample. Data processing, normalization and averaging was undertaken using the ProQEXAFS software.(2) Ex-situ pressed sample pellets were prepared by diluting with cellulose in order to give an absorption length of near one; however, since multiple energies were analyzed, the dilution was an average of the optimal dilution across the energy ranges.

Thermogravimetric analysis was performed on Netzsch STA 449 f3 Jupiter instrument in 600℃ with the heating rate of 10 ℃/min.

The magnetic properties of 8-cation LDH were studied with a Magnetic Properties Measurement System (MPMS 3, Quantum Design Inc.), equipped with an alternating current (AC) magnetic measurement option. The temperature dependent magnetization M(T) was measured between 5 K and 90 K, with external fields B = 0.005, 0.01, 0.1, and 1 T, respectively. The field-dependence of the magnetization M(H) was measured up to 7 T from 5 K to 90K. Moreover, FC memory and aging effects were measured by intermittent-stop cooling and continuous warming memory processes. In the intermittent-stop cooling process, the sample was cooled down from 90 K to 5 K in a field of 0.005 T with intermittent stops at, 50 K, 40 K, 30 K, 20 K, and 10K respectively. The field was switched off for 5000 s during stops, and then ramped up to 5 mT before cooling resumed. In the continuous warming memory process, the sample was measured in a field of 5 mT continuously from 5 K to 90 K. AC magnetization measurements were done from 5 K to 90K in zero direct magnetic field with peak amplitudes of 0.7 mT and frequencies of 1 Hz, 5 Hz, 10 Hz, 20 Hz, 50 Hz, 100 Hz, 300 Hz, respectively.

2. *Synthesis details for 8 cation and 7cat A-H*

Table S1: Extended synthesis details of masses used for solution preparation and final yields

Reactant	8 cation	7cat - A	7cat - B	7cat - C	7cat - D	7cat - E	7cat - F	7cat - G	7cat - H
Initial pH	2.0	2.1	1.9	2.1	2.0	1.9	2.0	1.9	2.4
Final pH	8.9	8.8	8.9	8.4	8.6	8.6	8.5	8.9	8.5
% Yield	73	75	88	87	80	79	76	84	78

Table S1: Extended synthesis details solution preparation and the resulting final yields.

Yield calculations based on a theoretical yield with an assumed LDH structure of $[M_{2/3}^{2+}M_{1/3}^{3+}(OH)_2]\ [CO_3]_{2/3}^{-2}$ where the product mass was measured after drying at 120°C for 16 hours. Yields may in reality be lower if water remained in the structure after drying.

3. *Additional synthesis*

a. *Synthesis of M(II)/M(III) with ratio 1 and 3 for 8 cation and 7cat-H*

Additional synthesis were carried out for tuning the M(II):M(III) ratio. The starting solution formulation for 8 cation and 7cat-H were adjusted for a M(II):M(III) ratio of 1 and 3. Molar amounts among the M(II) species were kept equivalent to each other, and similarly all M(III) were kept molar equivalent. All other hydrothermal synthesis parameters (2 hr at 150°C) were kept the same as samples with M(II)/M(III) of 2. Figure S1 shows the resulting XRD patterns. In the case of M(II)/M(III) is 3, small amount of impurities were observed at around 17.5 2theta. Formulation with M(II)/M(III) of 1, no impurities were detected.

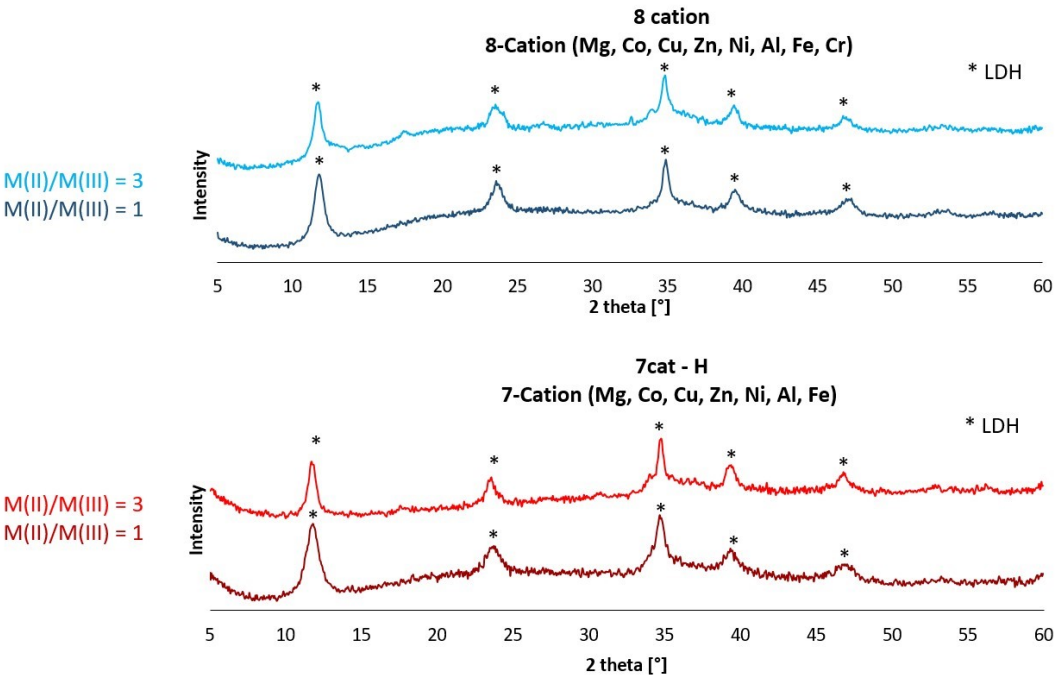

Figure S1: X-ray diffraction patterns of 8-cation and 7cat-H formulated with starting ratios of M(II)/M(III) of 1 and 3.

b. Synthesis of HE LDHs by precipitation (urea decomposition)

Additional synthesis test was conducted by the precipitation of HE-LDH by the decomposition of urea, rather than hydrothermally. The preparation of the salt solution for HEHs synthesis involved dissolving eight different nitrates and urea in 62,5 ml of distilled water, similarly to the hydrothermal synthesis method. In total, 38.7 grams of the solution was used for the experiment. The reaction temperature was set to 80℃ and rotation to 150 r/min. After 18 hours at 80℃, the solution was cooled to room temperature. The resultant precipitate was washed four times with distilled water and dried.

XRD analysis performed on the obtained powder confirmed the effectiveness of the hydrothermal synthesis method over the precipitating method. As shown in Figure S2, the powder received by precipitating method exhibited significant amount of impurities and exceptionally poor crystallinity. X-ray diffraction pattern of sample received by precipitating method indicated some characteristic for layered double hydroxides peaks, especially around value $2\theta = 11°$ and $2\theta = 35°$, however these peaks were not as high and sharp as in case of hydrothermal synthesis method.

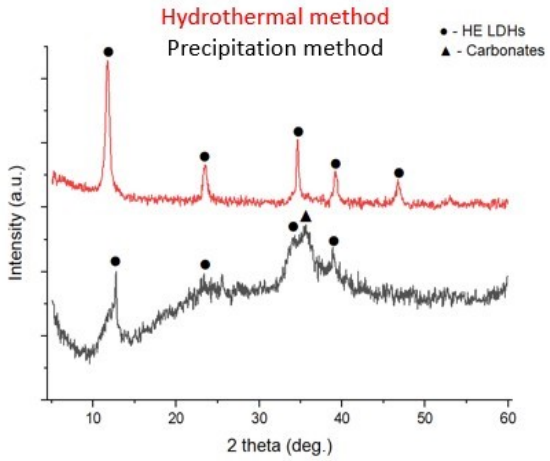

Figure S2: X-ray diffraction patterns of sample 2 powder obtained in precipitating and hydrothermal synthesis method.

The morphology obtained in precipitating method appeared to be considerably distinct from the morphology of the material resulting by the hydrothermal synthesis method. There was almost no presence of platelets-like agglomerates noted, which was characteristic for all samples derived by hydrothermal. These agglomerates were found in very limited quantities, noticeable only in certain parts of the sample. EDS analysis showed a tendency to segregation, especially for copper. Another difference between the two methods was observed in the incorporation of magnesium – in the case of the precipitating method atomic concentration of this element was equal only approximately 1.5.

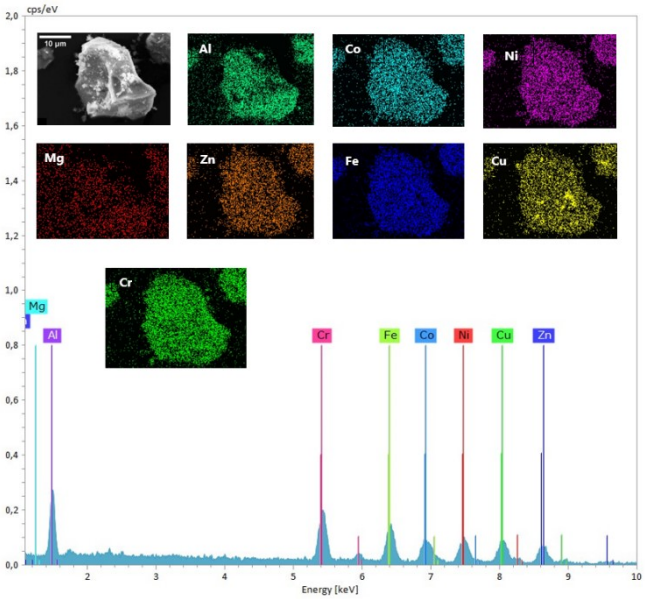

Figure S3: EDS mapping and spectra of sample 2 derived by precipitating method. Copper mapping shows large copper segragation phases.

Table S2. EDS analysis of atomic concentration of elements in sample 2 derived by precipitating method.

Sample	Atomic concentration (%)								Final M^{2+}/M^{3+} Ratio
	Mg	Zn	Cu	Ni	Co	Al	Fe	Cr	
2 Precipitating method	1.5	13.7	15.2	13.2	10.3	18.2	13.9	14.1	1

c. 9- cation synthesis

Synthesis was also conducted on a 9 - cation formulation (Mg, Zn, Cu, Co, Mn, Ni, Al, Cr, Fe) with synthesis conditions 150ºC and 2 hrs. X-ray powder diffraction pattern of the synthesized material shows that LDH forms along with carbonates. For the 9-cation formulation or more,

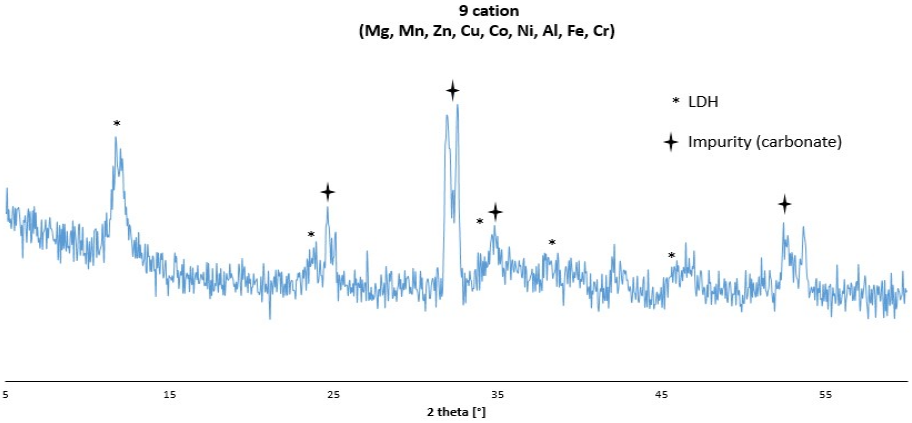

Figure S4: X-ray powder diffraction of 9-cation formulation synthesized at 150C for 2 hours. LDH is observed; however, a large carbonate phase is also present.

further synthesis and optimization is needed to synthesize pure LHD. The synthesis conditions for 7 and 8 cation appear to be not optimal for the incorporation 9 or more cations.

4. *Additional characterization of 8 cation and 7cat-H samples*

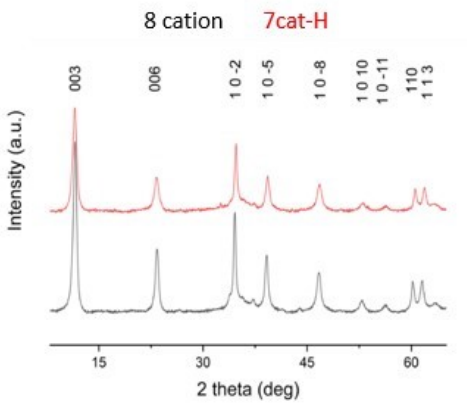

Reflection	2 theta (deg)		FWHM (°)		Peak Area
	8 cation	8-cation minus 7cat-H	8cation	8-cation minus 7cat-H	8-cation minus 7cat-H (%)
003	11.55	-0.04	0.57	+0.06	-31.2
006	23.35	-0.05	0.54	+0.17	-33.0
10 -2	34.54	+0.17	0.03	+0.05	-7.6
10 -5	39.13	+0.15	0.47	+0.11	-49.5
110	60.16	+0.35	0.40	+0.04	-19.0
113	61.49	+0.35	0.54	+0.01	-24.4

Figure S5: High resolution x-ray powder diffraction analyzed in transmission mode. Table (right) shows difference in the full width at high maximum (FWHM) between sample 8 cation and 7cat-H, as well as the difference in the peak areas.

a. *X-ray Powder diffraction*

Where k is shape factor (0,9) and λ is X-ray wavelength (0,154 nm) crystallite sizes were calculated (Table S3) using the Scherrer equation on reflection 003 and 006.

Table S3: Calculated crystallite sizes for sample 2 and 9 using the Scherrer equation.		
	8 cation	7cat - H
Reflection	Size (nm)	Size (nm)
003	14.0	12.7
006	15.0	11.4

b. EDS maping of 7cat-H (Mg, Zn, Cu, Co, Ni, Al, Fe)

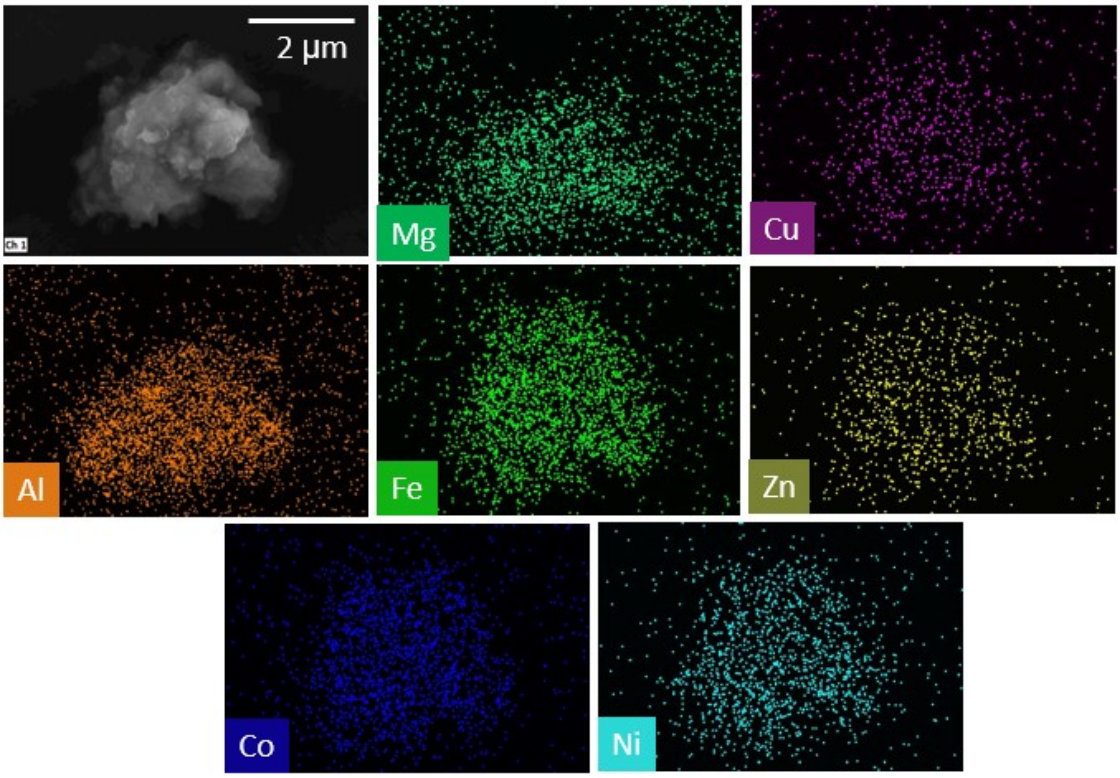

Figure S6: EDS spectra and mapping of 7-cation LDH.

c. Thermogravimetric analysis

In order to understand any difference between high entropy hydroxides and a Mg-Al hydrotalcite from similar synthesis conditions, thermal gravimetric (TG) analysis was conducted on samples 8 cations, 7cat-H and a hydrotalcite. Figure 5 illustrates TG curves of pure MgAl – CO_3 hydrotalcite and high entropy layered double hydroxides. As seen in Fig. 5a, as well as reported in the literature (3,4), hydrotalcites may undergo three major mass losses in three temperature ranges. In our material, the first decrease appeared between 100-210°C and was induced by loss of interlayer water and water absorbed over the material. The second weight loss occurred between 210-320°C and was related to initiation of dehydoxylation and removal of carbonate ions from interlayer space. This removal was also present in the last mass loss over 320°C, as well as decomposition of $MgCO_3$.

Despite the fact that hydrotalcites in general undergo two thermal transitions (5,6), each of these can appear in two steps. This may be influenced by, for instance, the ratio of divalent

to trivalent cations used, types of anions, or low temperature treatment such as a drying process (4,5). Further analysis of the two HE LDHs showed a similar location of the first considerable weight loss as in the case of MgAl-CO_3 hydrotalcite, that is, from 100-200°C approximately. A slight shift in the direction of lower temperatures was noticeable; however, this displacement was not significant. A major difference between hydrotalcite and HE LDHs was observed in the higher temperature range, starting from 200°C. For high entropy hydroxides, one large weight loss was noted, which in the case of the sample not containing chromium was shifted to the lower temperature range – about 40°C difference in comparison to the chromium–containing sample.

Thermogravimetric analysis confirmed that depending on the nature of the incorporated cations, the initiation of weight loss could begin at different temperatures, which is also consistent with literature findings regarding conventional layered double hydroxides (5).

Table S4. Results of weight losses of the TG for MgAl-CO_3 hydrotalcite and HE LDHs.

	Step 1		Step 2		Step 3		Total weight loss (%)
Sample	Temperature range (°C)	Weight loss (%)	Temperature range (°C)	Weight loss (%)	Temperature range (°C)	Weight loss (%)	
MgAl-CO_3 hydrotalcite	100 - 210	12.5	210 - 320	9.2	320 - 460	14.1	35.7
8 cation	100 - 190	6.9	190 - 370	16.9	-	-	23.8
7cat – H	100 - 195	6.5	195 - 330	13.3	-	-	19.8

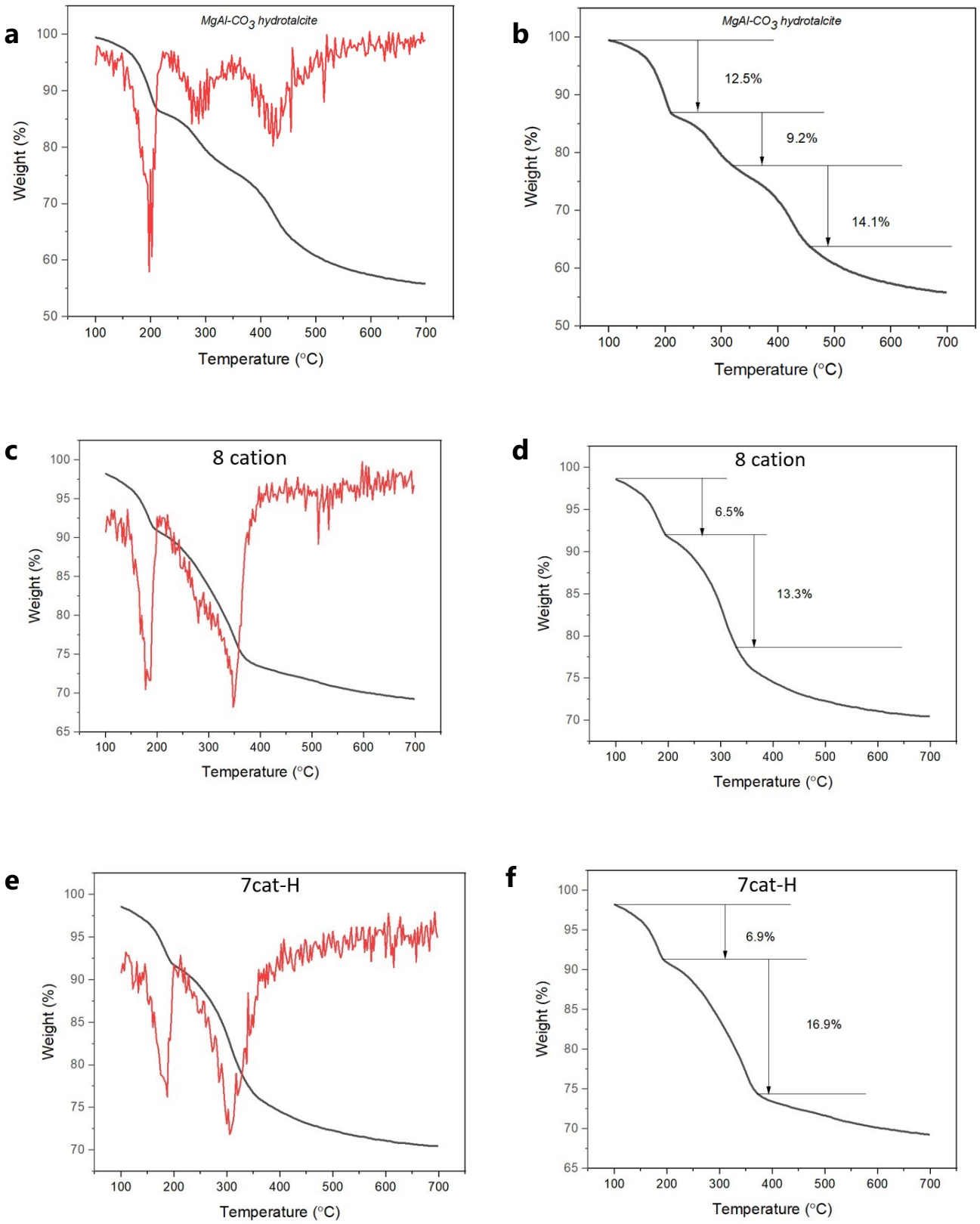

Figure S7. TG curves of MgAl – CO_3 hydrotalcite, 8-cation LDH, and 7 cation LDH (7cat-H). Red line indicates derivative of mass loss curve.

d. Ex-situ X-ray absorption analysis

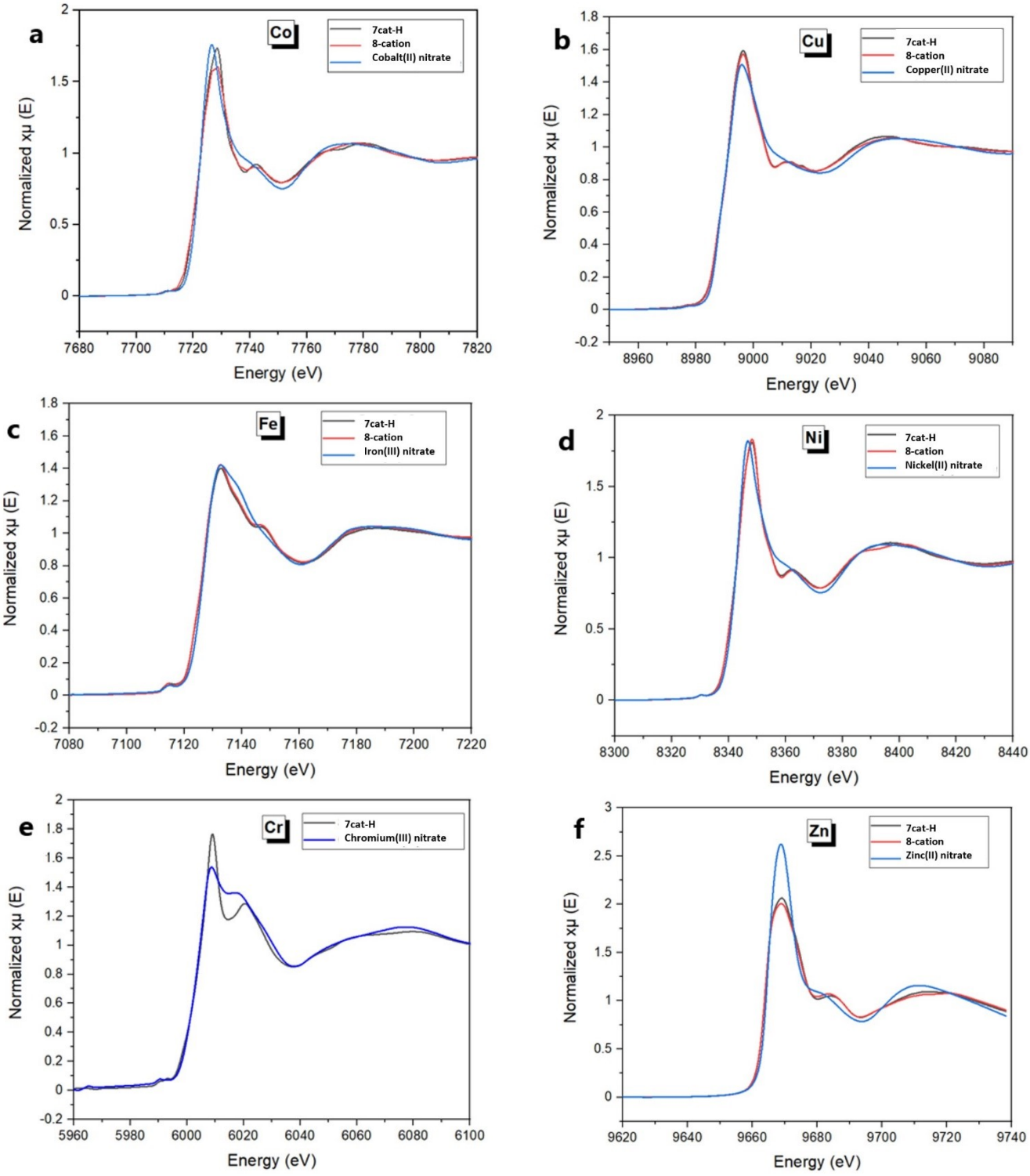

Figure S8. Normalized X-ray absorption spectroscopy data at the Co (a), Cu (b), Fe (c), Ni (d), Cr (e) and Zn (f) K-edge for precursors and reference compounds.

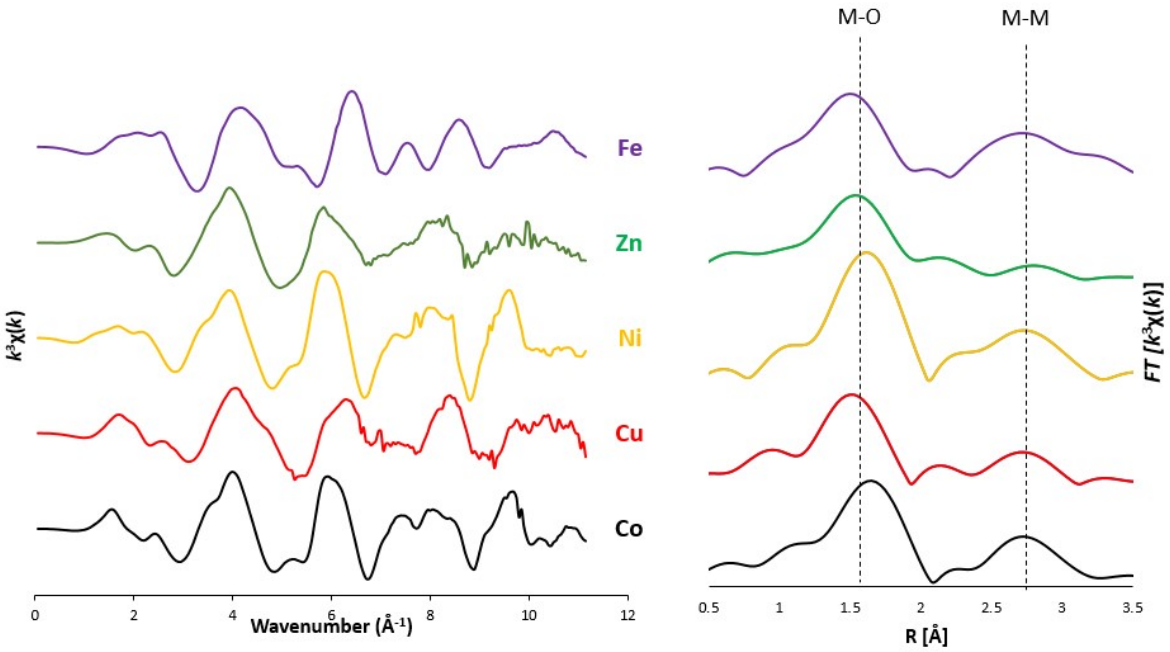

Figure S9. *(left)* Exafs spectra of Fe, Zn, Ni, Cu, and Co for 7-cation LDH. (*right*) The Fourier Transform of the k3χ(k) taken using the range of k= 2.5-10 Å-1. Scattering distances are uncorrected for phase-shift.

The amplitude reduction factor used in the fitting was determined to be 0.85 from fitting the Fe-foil reference and applied to all elements except chromium where an amplitude reduction factor of 0.75 was applied from the fitting of Cr-foil. Additional Cu-O scattering events from Jahn Teller distortions were also fitted; however, this led to poorer fittings.

e. Magnetization property measurements

Table S5: EXAFS fitting parameters and results for 8 cation LDH

Scatterer	Ni - O	Co - O	Cu – O	Zn - O	Fe - O	Cr - O
N	6.1 ± 0.7	6.0 ± 0.8	3.9 ± 0.	6.0 ± 0.7	5.5 ± 0.9	5.0 ± 0.9
R, Å	2.05 ± 0.01	2.06 ± 0.01	1.96 ± 0.01	2.03 ± 0.02	1.97 ± 0.02	1.98 ± 0.02
σ^2 , Å^2	0.005	0.007	0.007	0.01	0.01	0.001
Enot, eV	2.6	0.6	-6.5	3.8	-0.1	1.4
R factor	0.009	0.012	0.011	0.007	0.007	0.021

Table S6: EXAFS fitting parameters and results for 7 cation LDH (7cat-H)

Scatterer	Ni - O	Co - O	Cu – O	Zn - O	Fe - O
N	6.1 ± 0.9	5.5 ± 0.8	3.8 ± 0.3	5.5 ± 0.8	5.3 ± 0.8
R, Å	2.05 ± 0.02	2.07 ± 0.02	1.95 ± 0.8	2.03 ± 0.01	1.98 ± 0.02
σ^2 , Å^2	0.005	0.007	0.006	0.01	0.01
Enot, eV	-2.73	-3.4	-5.4	4.1	3.7
R factor	0.009	0.011	0.006	0.010	0.007

To analyze the frequency dependence of the $\chi'(T)$ peaks in the AC magnetization measurements, we use a critical dynamical scaling model in connection with the correlation length ζ ($\tau \propto \zeta^z$). It predicts a correlation between the measuring frequency $f = 2\pi/\tau$ and the peak temperature T in $\chi'(T)$ via

$$\tau = \tau_0 \left(\frac{T - T_s}{T_s}\right)^{-zv} \quad (1)$$

where T_s is the freezing temperature in the limit $\omega \rightarrow 0$ that is determined by the system interactions, z is the dynamic critical exponent, v is the exponent for the correlation length, and τ_0 is the flip time between relaxation attempts. The insert solid curve of Fig. 6a suggests that the magnetic behavior of 8-cation LDH can be well described by this critical dynamics scaling model with the fitted parameters: T_s = 30 ± 1 K, zv = 3.5 ± 0.9, and $\tau_0 \sim 10^{-5}$ s. The exponent value of zv is in the range of normal glassy systems with values in the range between 4 and 12 (7). Another criterion to analyze the frequency dependence of the χ' peaks is the Vogel-Fulcher model, which characterizes a continuous freezing crossover into a low-temperature glassy regime(8),

$$\tau = \tau_0 exp[E_a/k_B(T - T_0)] \quad (1)$$

where E_a is an energy barrier, k_B is the Boltzmann constant, τ_0 is the flip time, and T_0 is the characteristic temperature which is usually below the freezing temperature. In the insert of Fig. 7a, the dashed curve reveals that the Vogel-Fulcher model can describe the magnetic properties of the 8-cation LDH and with the parameters T_0 = 26 ± 2 K, $E_a/k_B \approx$ 56 K, and $\tau_0 \sim 10^{-5}$ s. The energy barrier is $E_a/k_B \sim 2T_s$ (T_s is obtained from fitting of the critical dynamics scaling model), as it is observed in other spin glasses(9).

In the intermittent-stop cooling process, the sample was cooled down from 90 to 5 K in a field of 5 mT, with intermittent stops at 50, 40, 30, 20 and 10 K respectively. In these stops, $\mu_0 H$ is switched off, followed by a waiting period of 5000 s at a constant temperature. Once the sample is in the spin-glass state, i.e., at 30, 20, and 10 K, the magnetization changes slowly from an initial remanent value with a time constant of several minutes (insert of Fig. 6b). After this process, the magnetic field is switched back to 5 mT, and the sample further cools down to the next temperature.

References

1. Müller O, Nachtegaal M, Just J, Lützenkirchen-Hecht D, Frahm R. Quick-EXAFS setup at the SuperXAS beamline for in situ X-ray absorption spectroscopy with 10ms time resolution. J Synchrotron Radiat. 2016;23:260–6.
2. Clark AH, Imbao J, Frahm R, Nachtegaal M. ProQEXAFS: A highly optimized parallelized rapid processing software for QEXAFS data. J Synchrotron Radiat. 2020;27:551–7.
3. Kanezaki E. Effect of Temperature on the Layered Structure of Hydrotalcite-like Mg and Al Layered Double Hydroxides by Means of in situ High Temperature Powder X-ray Diffraction. Hyomen Kagaku. 1998;19(5):288–93.

4. Rao MM, Reddy BR, Jayalakshmi M, Jaya VS, Sridhar B. Hydrothermal synthesis of Mg-Al hydrotalcites by urea hydrolysis. Mater Res Bull. 2005;40(2):347–59.
5. Cavani F, Trifirò F, Vaccari A. Hydrotalcite-type anionic clays: Preparation, properties and applications. Catal Today. 1991;11(2):173–301.
6. Zhitova ES, Greenwell HC, Krzhizhanovskaya MG, Apperley DC, Pekov I V, Yakovenchuk VN. Thermal Evolution of Natural Layered Double Hydroxides: Insight from Quintinite, Hydrotalcite, Stichtite, and Iowaite as Reference Samples for CO3- and Cl-Members of the Hydrotalcite Supergroup. Minerals. 2020;10:961.
7. Mydosh J a. Spin Glasses: An Experimental Introduction. Taylor Fr [Internet]. 1993; Available from: http://books.google.com/books?id=lRpmQgAACAAJ&pgis=1
8. Vogel H. The law of the relation between the viscosity of liquids and the temperature. Phys Z. 1921;22:645.
9. Mukherjee S, Garg A, Gupta R. Spin glass-like phase below ∼210 K in magnetoelectric gallium ferrite. Appl Phys Lett. 2012;100(11).